Composite Structures 322 (2023) 117327

Contents lists available at ScienceDirect

Composite Structures

journal homepage: www.elsevier.com/locate/compstruct

Dynamic characteristics and active vibration control effect for shape memory polymer composites

Peilei Xu [a], Xin Lan [b], Chengjun Zeng [a], Xudong Zhang [a], Yanju Liu [a,*], Jinsong Leng [b]

[a] Department of Astronautical Science and Mechanics, Harbin Institute of Technology, Harbin 150001, People's Republic of China
[b] Centre for Composite Materials and Structures, Harbin Institute of Technology, Harbin 150080, People's Republic of China

ARTICLE INFO

Keywords:
Shape memory polymer composite
Dynamic characteristics
Composite laminates
PID
Active vibration control

ABSTRACT

Shape memory polymer composites (SMPCs) are widely used as a new type of composite material in space expansion structures, which are prone to vibration and resonance in a space environment. A new type of macro fiber composite (MFC) can be used to control the vibration of the structure. Based on Kirchhoff plate theory, the differential equations of motion for composite laminates are derived. Theoretical analysis of SMPC cantilever plates with varying carbon fiber content is carried out. In addition, the effects of local temperature changes on the dynamic characteristics of SMPC with different fiber content are studied. The vibration differential equations of the SMPC cantilever plate were obtained by using the separation variable method and the modal vibration superposition principle. The state-space equations of the system were established based on the transfer function, and the frequency response was determined by sine sweep excitation of the SMPC specimen. The open-loop and closed-loop vibration active control of SMPC specimens was investigated using the classical proportional integral derivative (PID) procedure. Finally, the effect of carbon fiber content on the vibration active control characteristics of SMPC structures was analysed.

1. Introduction

In recent years, with many technical achievements and engineering applications in the field of space deployed structures in China, more and more large space structures are built with new intelligent materials. Shape memory polymer (SMP), as a novel deformable material, is able to transform between two shapes under the action of certain stimuli (heat, electricity, magnetism, light, solution, etc.) [1–4]. Since the discovery of SMPs in the last century, research on this new smart material has received increasing attention [5–8]. With the advantages of light weight, low cost, intelligent controllability, simple structure and high folding rate, SMPs has far-reaching application prospect in space expandable structure applications [9–11]. Epoxy-based SMPs have excellent properties in glass transition temperature, elastic modulus and deformation properties. However, the mechanical properties of epoxy SMP structures are poor and cannot be used directly as a base material for structures, such as spatial deformation [9] and spatial expansion [12]. SMPCs were formed by adding carbon fiber to the SMPs material to enhance its mechanical properties. [9,12].

Fiber-reinforced SMPC inherits both the shape memory properties of SMP materials and the high strength and stiffness properties of the fiber-reinforced phase. Their application in spatially expandable structures has gradually become a research hotspot in recent years [13,14]. The material-based telescopic structures can achieve very large expansion rates after folding, which makes the material-based structures suitable for space telescopic hinges, telescopic beams, trusses, antennas and other space telescopic structures in the aerospace field [15–18].

Typically, hinges are the most widely used drive component in deployable structures. Initially, Composite Technology Development, Inc designed the hinged form of Elastic Memory Composite and first applied it to solar arrays in 2006 [19]. In 2008, Liu et al. [20] designed a carpenter type hinge structure using the shape memory effect of SMPC. The carpenter type hinge performed excellently in repeated deployment experiments. By 2018, the SMPC hinge design had been improved. Liu et al. [21] designed and prepared a C-type slotted pipe integrated hinge based on SMPC. The hinges are installed by grooving and folding transversely at the joints. Finally, the structure can be extended by heating the hinges with different joints. In the same year, Herath et al. [16] manufactured a SMPC material and assembled it into a stepped deployable solar panel array. The SMPC hinge structures were tested in ground simulation of space environment in 2020 [22,23], which laid a solid foundation for the future deployment of SMPC structure. In 2022, Leng et al. [24] proposed an excellent synchronous deployment

* Corresponding author.
E-mail address: yj_liu@hit.edu.cn (Y. Liu).

https://doi.org/10.1016/j.compstruct.2023.117327
Received 21 March 2023; Received in revised form 15 May 2023; Accepted 4 July 2023
Available online 5 July 2023

Nomenclature

l	specimens' length
b	specimens' width
h	specimens' thickness
ρ	density of the SMPC
A_{ij}^*	Tensile stiffness
B_{ij}^*	Coupling stiffness
D_{ij}^*	Bending stiffness
$U(t)$	applied voltage
h_a	electrode spacing of the MFC actuator
h_m	thickness of the MFC actuator
x_1	position coordinates of the MFC actuator
x_2	position coordinates of the MFC actuator
x_3	excitation point of the shaker on the SMPC specimen
x_e	output point of the system
m_x	driving moment in the x-direction
M_x	internal bending moment in the x-direction of the plate
C_s	system damping
$\delta(x)$	Dirac function
ω_{ni}	i-th order natural frequency
M_i	modal mass of the structure
$z(t)$	a column vector consisting of modal displacements and modal velocities
$y(t)$	system output variable
A	system matrix
B	system control matrix
C	system output matrix
E_1	longitudinal Young's modulus of the carbon fiber reinforced epoxy layer
E_2	transverse Young's modulus of the carbon fiber reinforced epoxy layer
$f_i(t)$	bending moment under the modal shape
$F_i(t)$	exciting force under the mode shape
ζ	structural damping ratio
K_P^*	proportional coefficient
K_I^*	integral time constant
K_D^*	differential time constant
$G(s)$	transfer function
v_f	carbon fiber volume content
SMPCs	shape memory polymer composites
SMP	shape memory polymer
MFC	macro fiber composite
PID	proportional integral derivative
FFT	Fast Fourier Transformation

mechanism triggered by SMPC components. By 2023, Liu et al. [25] designed a self-deployable mechanism using SMPC for unfurling the national flag on a Mars rover, which verifies the enormous potential of SMPC in space applications.

At the same time, the application of fiber-reinforced SMPC space structures also face some problems. In general, previous research has focused on the intrinsic modeling of SMPC and improving its mechanical properties. Little research has been done on the dynamic characteristics and active vibration control of SMPC laminates. In the space environment, the expansion, posture adjustment and orbit adjustment of the space structures tend to make them vibrate and resonate at their intrinsic frequencies, which can easily have a destructive effect on the linking components of the space structure. Depending on the needs, different SMPC structures are often used as connectors and locking elements for the space structure.

Therefore, it is of great significance to investigate the dynamic characteristics of carbon fiber reinforced SMPC and to explore its active control characteristics of vibration. Firstly, the dynamic properties of the structure are obtained in this paper using the corresponding experimental methods based on theory and simulation. On this basis, open-loop control experiments were conducted for SMPC specimens with varying fiber contents to obtain the control effect of SMPC specimens under open-loop control. After that, swept-frequency vibration suppression experiments at low frequencies were conducted on SMPC specimens. Finally, the closed-loop vibration control effect of SMPC specimens under natural frequency vibration is investigated. This paper provides a reference for future research and application of SMPC in dynamic characteristics and active control of vibration.

2. Theory of SMPC with piezoelectric actuator

2.1. Constitutive equations

A new type of macro fiber composite (MFC) is used to control the vibration of the structure. Fig. 1 shows a SMPC laminate with an attached MFC actuator. One end of the SMPC is fixed and the other end is free. The length, width and thickness of the SMPC laminate are$l = 200$ mm, b=20 mm and$h = 3$ mm respectively.

The length and width of the structural model are much larger than the thickness dimension, which define the existence of a midplane for the thin plate. Since the vibration deformation of the structure is small relative to the size of the structure, the linear theory is used for theoretical modeling. The displacement of the structure is obtained from Kirchhoff plate theory. The thickness of each layer (setting the thickness direction as 3 directions) is generally small compared with the dimensions of the other in-plane directions (1, 2). Therefore, it can be approximated that $\sigma_3 = 0, \tau_{23} = 0, \tau_{31} = 0$. Considering no lateral load and ignoring the plane load, the free vibration equation of the plate is obtained.

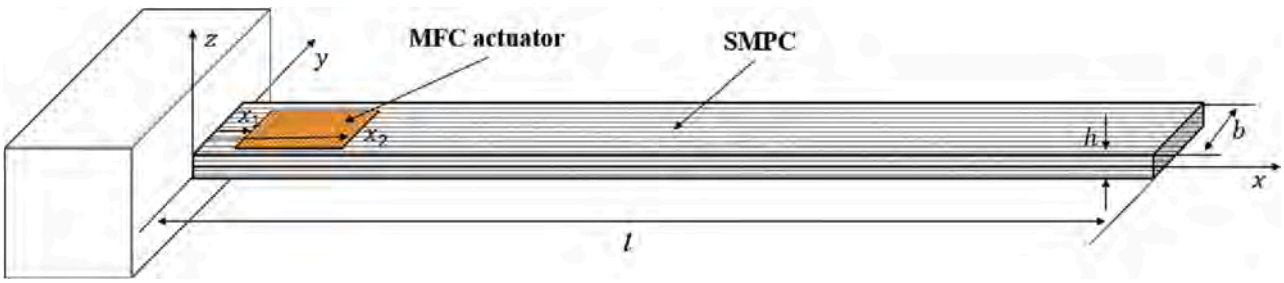

Fig. 1. Shape memory polymer composite laminate with MFC actuator.

$$D_{11}^{*}\delta w_{,xxxx}+2\left(D_{12}^{*}+2D_{66}^{*}\right)\delta_{,xxyy}+D_{22}^{*}\delta w_{,yyyy}+D_{16}^{*}\delta w_{,xxyy}+4D_{26}^{*}\delta w_{,xyyy}+\rho h\delta w_{,tt}=0, \tag{1}$$

Considering that the shape memory polymer composite laminate is an orthotropic plate,$B_{ij}^{*}=0$, $A_{16}^{*}=A_{26}^{*}=D_{16}^{*}=D_{26}^{*}=0$ can be used to obtain the differential equation for the motion the thin plate microelement:

$$D_{11}^{*}\delta w_{,xxxx}+2\left(D_{12}^{*}+2D_{66}^{*}\right)\delta_{,xxyy}+D_{22}^{*}\delta w_{,yyyy}+\rho h\delta w_{,tt}=0, \tag{2}$$

The variables to be solved include time t and coordinates x and y, and the variable separation formula is obtained.

$$w(x,y,t)=W(x,y)\cos(\omega t+\varphi), \tag{3}$$

The solution is assumed to have the following form [26]:

$$W(x,y)=X(x)Y(y), \tag{4}$$

The x direction can be regarded as a cantilever structure. The y direction can be regarded as a free structure at both ends. At the same time, considering the narrow width of the study cantilever plate, the aspect ratio of the cantilever plate reaches 10:1. When both ends are free (corresponding to translational motion), $\omega_0=0$ is satisfied in this direction, and combined with the boundary conditions, it can be determined that

$$Y_0(y)=a_1+a_2y, \tag{5}$$

Meanwhile, it can be obtained from Equation (4)

$$W(x,y)=\sum_{m=1}^{\infty}\sum_{n=1}^{\infty}A_{mn}X_m(x)Y_n(y), \tag{6}$$

where X_m and Y_n are given in Appendix A.

Putting the above formula into the differential equation of motion, the k-th natural frequency can be obtained as follows:

$$\omega_k=\frac{(k_ml)^2}{l^2}\sqrt{\frac{D_{11}}{\rho h}}, \tag{7}$$

where k_ml is the kth eigenvalue of the vibration equation.

2.2. Governing equation

The inverse piezoelectric effect property of piezoelectric materials gives them the ability to convert electrical energy into mechanical energy. Using this property, piezoelectric materials can also be used as actuators. The stress–strain relationship of the structure is complex during the whole process. For accurate force calculation during subsequent control, it is assumed that the MFC sheet is ideally attached to the SMPC surface and that the stress transfer between the MFC and SMPC is continuous and without loss. Considering that the strain in the length direction of the SMPC is much larger than the strain in the width direction, ignoring the strain in the width direction, the magnitude of the stress and strain induced by the MFC actuator is

$$\begin{cases}\sigma_x=E_m(\varepsilon_x+d_{33}E_x),\\ \varepsilon_x=\dfrac{d_{33}U(t)}{h_a},\end{cases} \tag{8}$$

where $U(t)$ represents the applied voltage, h_a represents the electrode spacing of the MFC actuator. The MFC actuator is pasted near the root of the SMPC, and the driving moment expression of the MFC to the SMPC is expressed as follows:

$$m_x=\int_{h/2}^{h+h_m/2}by\sigma_x dy, \tag{9}$$

where h_m represents the thickness of the MFC actuator.

Since the thickness of the MFC actuator is much smaller than that of the SMPC specimen, the approximate driving moment in the x-direction can be expressed as follows [27]:

$$m_x=bh_mE_md_{33}U(t)(h/2+h_m/2)/h_a=PU(t)[H(x-x_1)-H(x-x_2)] \tag{10}$$

where H(step) represents the unit Heaviside (step) function, x_1 and x_2 represent the position coordinates of the MFC actuator.

Considering the narrow width of the study cantilever plate, the aspect ratio of the cantilever plate reaches 10:1. The width of the MFC brake is approximately equal to that of the cantilever plate. Therefore, the effect of the MFC brake on the y-direction is not considered. Assuming that the MFC actuator has no significant effect on the dynamics of the SMPC board, the equation of motion is

$$\frac{\partial^2(M_x-m_x)}{\partial x^2}-C_s\dot{\omega}-\rho h\ddot{\omega}=0 \tag{11}$$

where M_x is the internal bending moment in the x-direction of the plate.

$$M_x=-\left(D_{11}^{*}\frac{\partial^2\omega}{\partial x^2}+D_{12}^{*}\frac{\partial^2\omega}{\partial y^2}\right) \tag{12}$$

The equation of motion is obtained as follows:

$$D_{11}^{*}\frac{\partial^4\omega}{\partial x^4}+C_s\dot{\omega}+\rho h\ddot{\omega}+PU(t)[\delta'(x-x_1)-\delta'(x-x_2)]=0 \tag{13}$$

where C_s is the system damping, ρ is the density of the SMPC and $\delta(x)$ is the Dirac function.

According to the modal vibration superposition principle, the equations of motion of the structure are represented by a linear combination of the main modal vibration modes of the system.

$$\omega(x,t)=\sum_{i=1}^{n}W_i(x)r_i(t)=W(x)^Tr(t) \tag{14}$$

where $W_i(x)$ represents the i-th order structural mode shape of the cantilever beam system, and $r_i(t)$ represents the i-th order modal coordinate.

The vibration differential equation for the SMPC system in modal coordinates is given by

$$\ddot{r}_i(t)+2\zeta_i\omega_{ni}\dot{r}_i(t)+\omega_{ni}^2r_i(t)=f_i(t)/M_i \tag{15}$$

where ζ_i represents the structural damping ratio, ω_{ni} represents the i-th order natural frequency.

(1) For the MFC actuator, $f_i(t)$ represents the bending moment under the modal shape, which can be expressed as follows:

$$\begin{aligned}f_i(t)&=\int_0^l\frac{\partial^2}{\partial x^2}(m_x)W_i(x)dx=\int_0^lPU(t)[\delta'(x-x_1)-\delta'(x-x_2)]W_i(x)dx\\&=PU(t)\left(W_i'(x_2)-W_i'(x_1)\right),\end{aligned} \tag{16}$$

where M_i is the modal mass of the structure.

$$M_i=\int_0^l\rho AW_i^2(x)dx,\ i=1,2\ldots \tag{17}$$

The Laplace transform on both sides of the equal sign of the vibration differential equation, it can be obtained as follows:

$$\left(s^2+2\zeta_i\omega_{ni}+\omega_{ni}^2\right)Q_i(s)=PU(t)\left(W_i'(x_2)-W_i'(x_1)\right)/M_i \tag{18}$$

The transfer function can be expressed as follows:

$$H_i(s)=\frac{Q_i(s)}{U(t)}=\frac{P\left(W_i'(x_2)-W_i'(x_1)\right)}{M_i(s^2+2\zeta_i\omega_{ni}+\omega_{ni}^2)} \tag{19}$$

Introduce state quantities:

$$z(t) = [\,r \quad \dot{r}\,]^T = \left[\, r_1(t) \quad r_2(t) \quad \cdots \quad r_n(t) \quad \dot{r}_1(t) \quad \dot{r}_2(t) \quad \cdots \quad \dot{r}_n(t) \,\right]^T \tag{20}$$

According to this transfer function, the state space equation of the system can be obtained:

$$\begin{cases} \dot{z}(t) = Az(t) + Bu(t) \\ y(t) = Cz(t) \end{cases} \tag{21}$$

where $z(t)$ is a column vector consisting of modal displacements and modal velocities and $y(t)$ is the system output variable. The system matrix A, B and C is given in Appendix B.

(2) For the shaker, the motion equation of the system is expressed as follows:

$$D_{11}^{*}\frac{\partial^4 \omega}{\partial x^4} + C_s\dot{\omega} + \rho h\ddot{\omega} = F(t)\delta(x - x_3) \tag{22}$$

The vibration differential equation for the SMPC system in modal coordinates is given by

$$\ddot{r}_i(t) + 2\zeta_i\omega_{ni}\dot{r}_i(t) + \omega_{ni}^2 r_i(t) = F_i(t)/M_i \tag{23}$$

$F_i(t)$ represents the exciting force under the mode shape:

$$F_i(t) = \int_0^l F(t)\delta(x - x_3)W_i(x)dx = F(t)W_i(x_3) \tag{24}$$

The Laplace transform on both sides of the equal sign of the vibration differential equation, it can be obtained:

$$\left(s^2 + 2\zeta_i\omega_{ni} + \omega_{ni}^2\right)R_i(s) = F(s)W_i(x_3)/M_i \tag{25}$$

Its transfer function can be expressed as follows:

$$T_i(s) = \frac{R_i(s)}{F(t)} = \frac{W_i(x_3)}{M_i(s^2 + 2\zeta_i\omega_{ni} + \omega_{ni}^2)} \tag{26}$$

where x_3 is the excitation point of the shaker on the SMPC specimen.

According to this transfer function, the state space equation of the system is can be obtained:

$$\begin{cases} \dot{z}(t) = Az(t) + Bu(t) \\ y(t) = Cz(t) \end{cases} \tag{27}$$

where $z(t)$ is a column vector consisting of modal displacements and modal velocities and $y(t)$ is the system output variable. The system matrix A, B and C is given in Appendix C.

2.3. Simulation model

Finite element analysis of SMPC specimens with different fiber contents was carried out using ABAQUS finite element simulation software. The basic mechanical parameters of carbon fiber layer and pure epoxy matrix layer at room temperature are shown in the Table 1 and Table 2. The density of the SMPC is approximately 1500 kg/m^3. The density of the pure epoxy matrix is about approximately 1000 kg/m^3.

To improve the fineness of the mesh and reduce the error between the simulation results and real situation, the SMPC structure was used in the simulation process with a shell structure. The simulation model is meshed by quadrilateral linear elements (S4R) and the approximate global mesh size of the model has been set to 0.0005 m. The model is meshed into about 16,000 elements. A sensitivity analysis was also performed on the number of finite element model meshes, and the statistical results are shown in Table 3. The fixed end of the SMPC structure is completely constrained, and the modal analysis is performed using the solution-type normal mode. Lanczos is used as the eigenvalue extraction method, and the expected number of roots is 5.

Table 1
Material parameters for the carbon fiber reinforced epoxy layer.

Parameters	E1/GPa	E2/GPa	Poisson's ratio	Shear modulus /GPa
value	30	2.8	0.35	1.5

Table 2
Material parameters for the epoxy resin matrix.

Parameters	Tensile modulus /GPa	Poisson's ratio	Shear modulus /GPa
value	2	0.38	0.725

3. Preparation

The SMPC laminates were prepared by protective molding process using shape memory epoxy resin and curing agent developed by Leng Jinsong's class group at Harbin Institute of Technology [28] and T300-3 K unidirectional fiber cloth as carbon fiber. The SMPC specimens were cut into 220 mm × 20 mm × 3 mm (the clamping part of the fixture is 20 mm) by the engraving machine. The thickness of each carbon fiber layer is 0.2 mm, and the mechanical properties and density of each carbon fiber layer and shape memory epoxy matrix are shown in Table 1. At the same time, the elastic modulus, shear modulus and Poisson's ratio can be obtained through Voigt's isostrain assumption.

To avoid the influence of gravity on the experimental results, the fixed end of the SMPC specimen was vertically fixed on a fixed table for frequency response analysis. As show in Fig. 2,the drop-shaped accelerometer (PCB PIEZOTRONICS LW254351) is attached to the free end of the SMPC specimen to test the acceleration of the free end of the specimen, and a laser rangefinder (Panasonic Industrial Devices SUNX SERIAL NO. JE8053) is used to test the displacement of the free end of the experimental specimen. The shaker (JZK-10) excites the SMPC at a distance of 10 mm from the fixed end. A signal generator (KEYSIGHT 33500B) is used to excite and actively control the vibration of the SMPC structure through the use of a power amplifier (YE5872 POWER AMPLIFIER) and an MFC signal amplifier (High Voltage Amplifier HVA1500/50). The signals are calculated and programmed using the LabVIEW operating platform in the PXIe chassis (number of slots of 6, maximum bandwidth of 2 GB/s, and a system bandwidth of 8 GB/s), the analog input card (8 channels, 24 Bit, 204.8Ks/s) and the analog output card (32 channels, 16 Bit, 2 Ms/s). (SEE Fig. 3.Fig. 4.).

The dynamic characteristics of the SMPC specimens were obtained by sweeping the excitation frequency of the shaker on the SMPC specimens and studying the variation law of the forced vibration response of the SMPC structure with the excitation frequency. To accurately test the dynamic characteristics of SMPC specimens, a droplet accelerometer and a laser positioner were used to simultaneously collect vibration data from SMPC specimens. The acquired data were subjected to Fast Fourier Transformation (FFT) to obtain the intrinsic frequencies of the SMPC specimens.

The free decay method was used to test the damping ratio of SMPC specimens. After mounting the SMPC specimen on the fixture, the acceleration sensor and laser positioner are installed on the SMPC specimen. Each SMPC specimen is hammered 5 times with a force hammer, and the data are measured by using an acceleration collector and a laser locator. The damping ratio of the SMPC specimen was obtained by analyzing the vibration waveform of the free end of the SMPC specimen. The system damping:$C_s = 2\zeta\omega_n$, damped natural frequency: $\omega_d = \omega_n\sqrt{1-\zeta^2}$, decrease factor $\eta = A_i/A_{i+1} = e^{\zeta\omega_n T_d}$, and $\delta = 1/j + \ln(A_j/A_{j+1}) = \zeta\omega_n T_n = \zeta\omega_n 2\pi/\omega_d = \zeta\omega_n 2\pi/\sqrt{1-\zeta^2}$. The damping ratio is $\zeta = \delta/\sqrt{(2\pi)^2 + \delta^2}$.

The end displacement of the specimens as measured by the acquisition device is used as the feedback signal, and the MFC piezoelectric material is used as the actuator to control the SMPC structure. In order to

Table 3
Sensitivity analysis of element number.

Element number	10	40	99	250	469	1000	4000	16,000
	Natural frequency/Hz							
v_{f1}	25.603	25.469	25.497	25.498	25.498	25.498	25.497	25.497
v_{f2}	35.776	35.599	35.608	35.608	35.607	35.607	35.607	35.607
v_{f3}	42.925	42.720	42.727	42.727	42.726	42.726	42.725	42.725
v_{f4}	49.783	49.550	49.552	49.551	49.551	49.550	49.550	49.549
v_{f5}	52.484	52.240	52.242	52.240	52.239	52.239	52.238	52.238

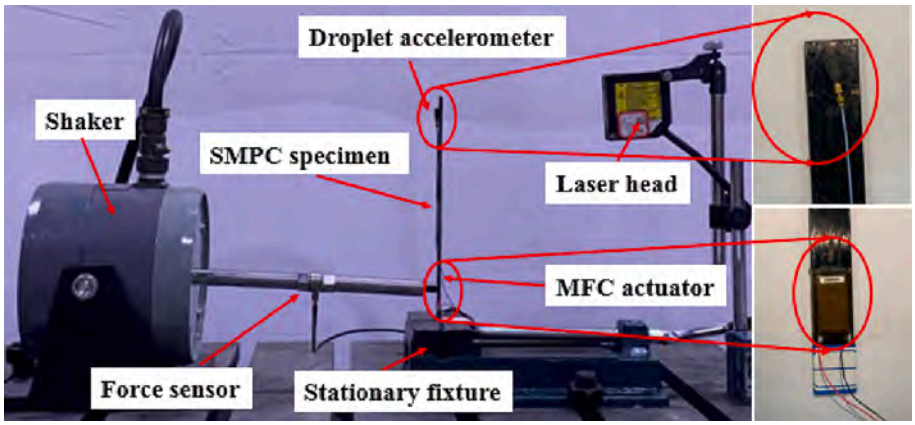

Fig. 2. Layout and operation diagram of the experimental equipment.

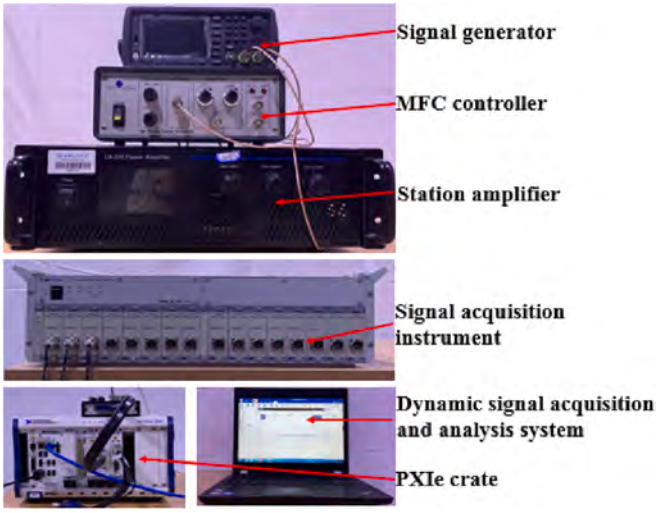

Fig. 3. Experimental equipment drawing.

maximize the effect of MFC, the MFC actuator is affixed to the root of the SMPC specimen and the vibration of the SMPC specimen is controlled by the input signal for classical PID control. Classical PID control has a simple control principle, easy software programming, and is highly adaptable in all areas of industrial control. Its robustness is good, and the control object is less affected by external interference, and can adapt to most of the harsh environments [29]. The active control adopts closed-loop control, which can sense the excitation response of the structure in real time and output the corresponding control force to achieve the desired control purpose.

In the control process, the PID control compares the feedback value of the actual output value $y(t)$ according to the given value $r(t)$ to form the control deviation $e(t)$, that is, $e(t) = y(t) - c(t)$. The proportional element (P), integral element (I) and differential element (D) for $e(t)$ are linearly combined to form the output $u(t)$ of the controller, which controls the controlled object.

$$u(t) = K_P^* e(t) + K_I^* \int_0^t e(t)dt + \frac{K_D^* de(t)}{dt} \tag{28}$$

where K_P^*, K_I^* and K_D^* represent the proportional coefficient, the integral time constant and the differential time constant.

The transfer function is given by

$$G(s) = \frac{U(s)}{E(s)} = K_P^* \left(1 + \frac{1}{T_I^* S} + T_D^* S\right) \tag{29}$$

4. Results and discussion

4.1. Dynamic characteristic analysis

For the obtained damping oscillation waveform, 7 consecutive amplitudes are arbitrarily selected and calculated as follows:

$$\delta_i = \frac{1}{7} + \ln \frac{A_1}{A_7}; \zeta_i = \frac{\delta_i}{\sqrt{(2\pi)^2 + \delta_i^2}}, \tag{30}$$

Based on the free attenuation method, the damping of SMPC specimen was obtained, as shown in Fig. 5. The figure shows that the damping ratio of SMPC specimen containing carbon fiber is lower than that of pure epoxy specimen. This is because the damping properties of composites are mainly derived from the viscoelasticity of the polymer matrix and the interaction between the fibers and the matrix. For composites with unidirectional fibers, the viscoelasticity of the polymer matrix plays a larger role in the damping properties of the composite. Therefore, as the carbon fiber content increases, the polymer matrix content of the SMPC specimen decreases, which leads to a decrease in the damping ratio of the specimen. Finally, the damping ratio calculation results are applied to the theoretical and simulation analysis.

To improve the fineness of the mesh and reduce the error between the simulation results and real situation, the SMPC structure adopts the shell structure in the simulation process. Lanczos is used as the eigenvalue extraction method, and the expected number of roots is 5. The

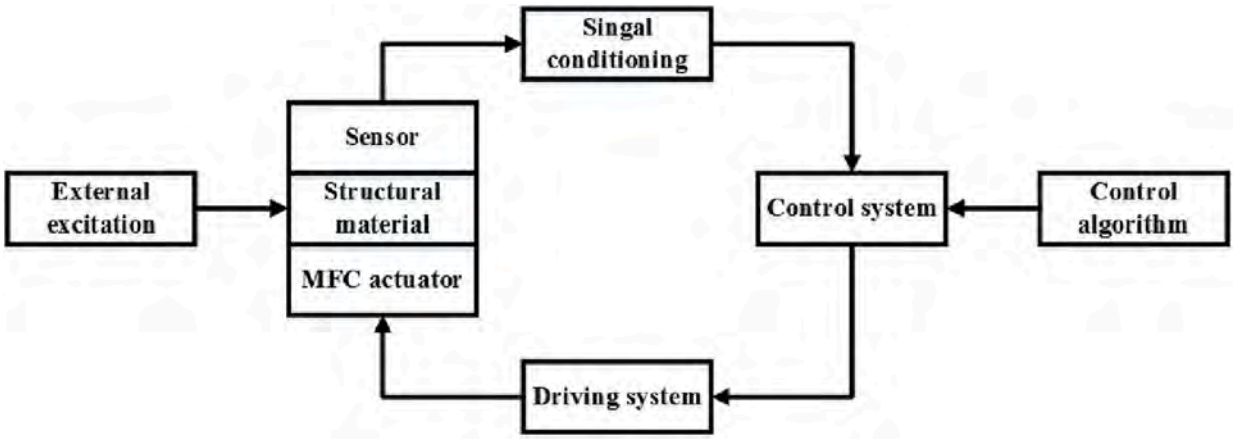

Fig. 4. Block diagram of the intelligent structural vibration active control system.

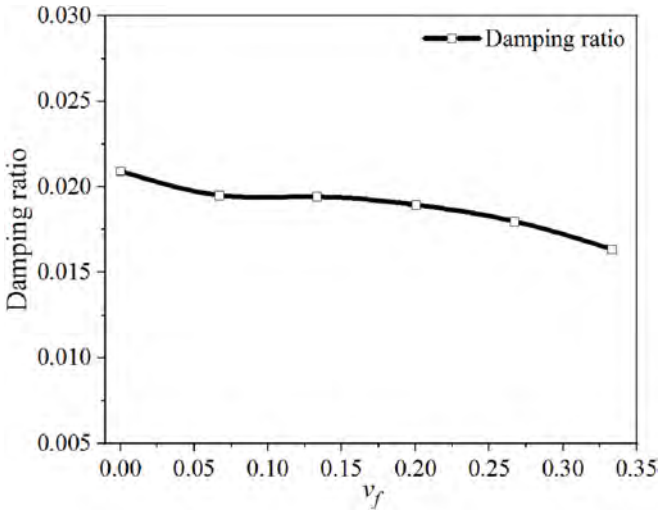

Fig. 5. Damping ratio for the SMPC specimens.

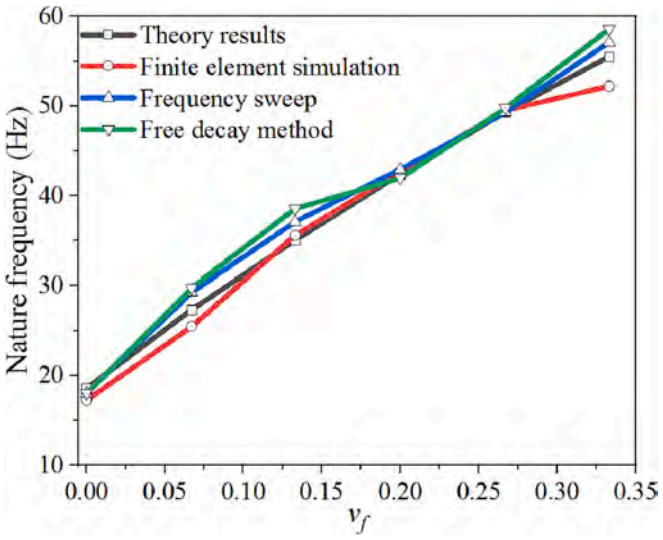

Fig. 7. The natural frequency theory and experimental data for SMPC specimens.

mesh model and the first-order frequency model are shown in Fig. 6. The first-order modal deformation map clearly shows the region of deformation and motion for the structure. The above theoretical formula was used to calculate the intrinsic frequency of SMPC, and the calculated results and experimental data are shown in Fig. 7.

The SMPC specimens were tested by theoretical calculations, finite element simulations, swept frequency experiments and free decay method experiments. Fig. 7 shows the theoretical calculation results are in good agreement with the experimental results, proving the accuracy of the experimental data. As the carbon fiber content in the SMPC specimens increases, the natural frequency of the SMPC structure presents a linear upward trend. This is because the stiffness of the carbon fiber reinforced epoxy layer of the SMPC specimen is much greater than the stiffness of the composite matrix. The variation of fiber content of SMPC specimens has a greater effect on the structural stiffness.

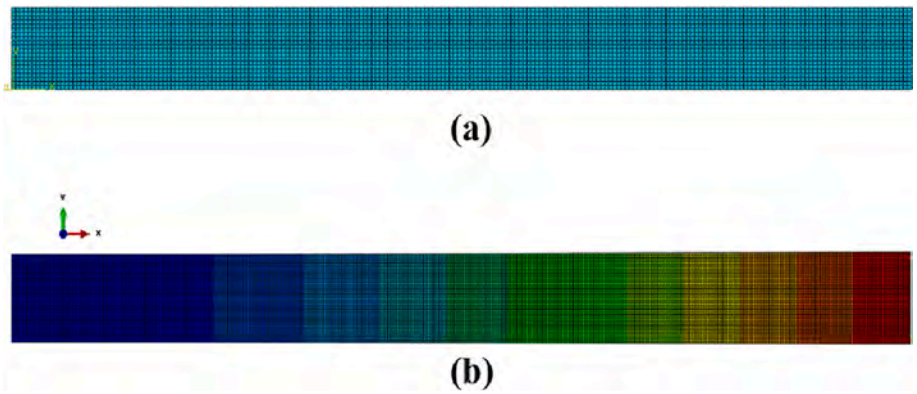

Fig. 6. (a) The finite element mesh model, (b) the first-order bending mode of the cantilever beam.

Therefore, with the increase of v_f, the stiffness of SMPC specimen increases, leading to the increase in the natural frequency of the specimen.

To confirm the correctness of the transfer function theoretical model for the SMPC specimens, the frequency response Bode diagram for the SMPC specimens is given. It can be seen from Fig. 8 that the frequency and amplitude for the wave peaks for the SMPC specimens ranging from v_{f1} to v_{f5} are determined to be 27.3 Hz, −59.2 dB; 35.2 Hz, −64 dB; 42.4 Hz, −66.9 dB; 49.3 Hz, −69.4 dB; 55.5 Hz, −70.9 dB. From the obtained results, it can be seen that the peak transverse coordinate of the frequency response function is consistent with the intrinsic frequency calculated using the theoretical formula. The symbols v_{f1} , v_{f2} , v_{f3} , v_{f4} , and v_{f5} represent the SMPC samples with carbon fiber volume contentsv_f = 0.067, 0.133, 0.200, 0.267 and 0.333, respectively.

The excitation frequency range of the shaker input signal is 0 ~ 200hz, covering the first order resonant frequency of the SMPC structure. The ratio of the free end displacement to the fixed end input force is used to obtain the frequency response function (FRF), which is used to calculate the response of the SMPC. The results show that the numerical simulation at low frequency agrees well with the measured frequency response results. The horizontal coordinate of the first resonance peak of the frequency response function corresponds to the natural frequency of the SMPC specimen. Meanwhile, the transverse coordinate of the first resonance peak of the experimental frequency response function increases with the increase of the carbon fiber content v_f of the SMPC specimen.

The trend of the curve shown in Fig. 9 shows that the peak value of the FRF corresponds to the natural frequency of the SMPC specimens. At this frequency, a small excitation can easily excite the structure. When the frequency exceeds the peak frequency of the SMPC specimen, the amplitude of the FRF shows a downward trend. At frequencies where the amplitude of the FRF is small, the structure is difficult or impossible to excite. At the same time, the figure shows that the SMPC specimen of v_{f1} exhibits a second peak at 170 Hz, which corresponds to its second-order frequency. The second-order frequencies for the SMPC specimens with other fiber contents all exceed 200 Hz, so they are not shown in the figure. (SEE Fig. 10.Fig. 11.).

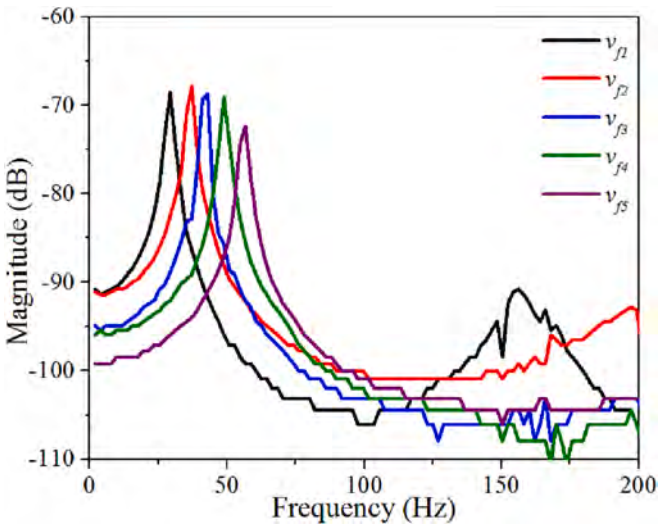

Fig. 9. Experimental frequency response curves for the SMPC specimens.

4.2. Dynamic characteristic analysis at different temperature

As a link structure of spatial structure, SMPC is often unfolded in a heat-driven manner. The extended link structure will remain heated for a certain period of time, so the dynamic characteristics of SMPC specimens at different temperatures need to be studied. The electric heating film pasted on the SMPC specimen was used to realize the local heating of the SMPC. The size of the heating film is 50 mm × 20 mm, and$m$ = 75 mm,n = 125 mm.

The local temperature of SMPC was controlled by thermistor and temperature controller. The dynamic properties of the specimens were obtained by hammering method based on temperature control. Due to the existence of unavoidable factors such as experimental error, each specimen was hammered several times and the obtained results were averaged. It can be observed from Fig. 12 that the effect of temperature on the specimen is inversely proportional to the fiber content in the specimen after considering the local temperature variation. This is

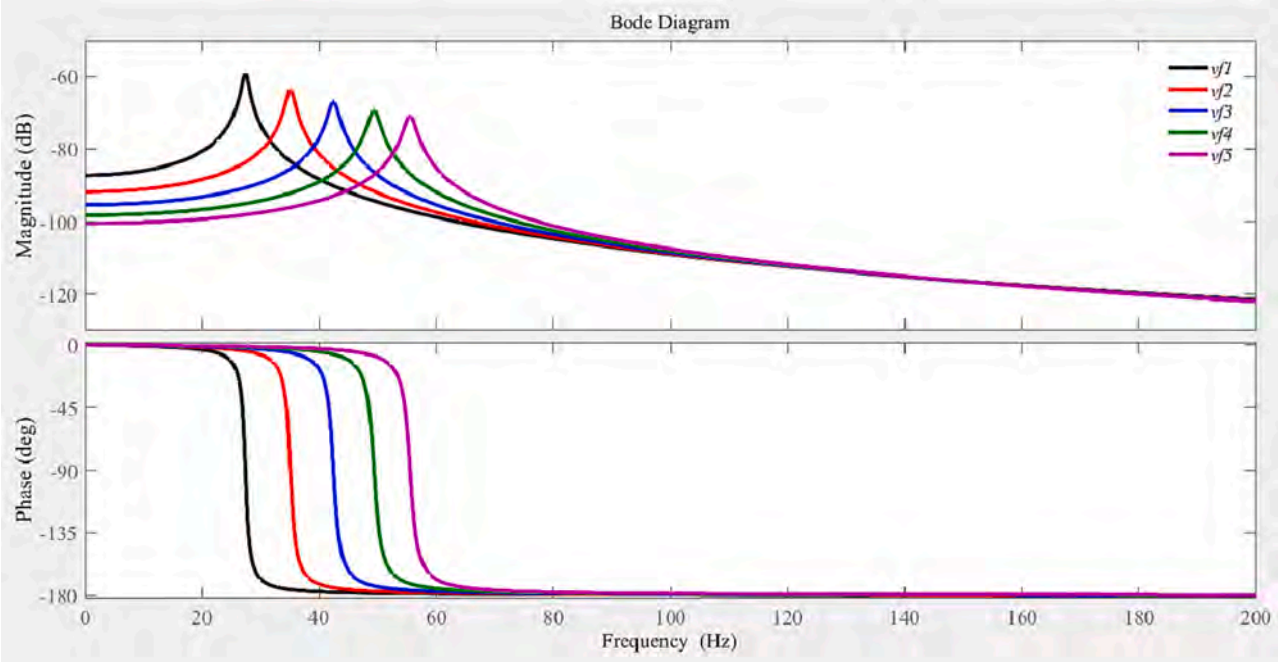

Fig. 8. Bode diagram of the transfer function for SMPC specimens.

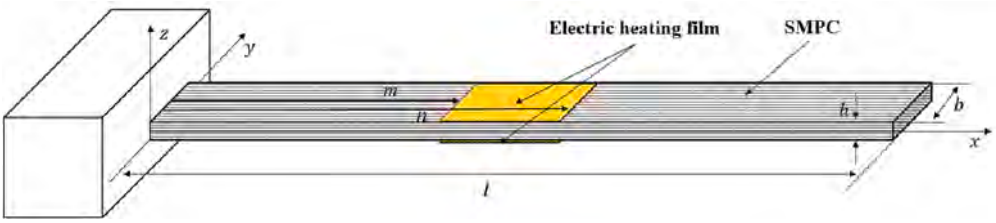

Fig. 10. SMPC specimen with electric heating film.

Fig. 11. Physical picture of SMPC specimen with electrothermal film.

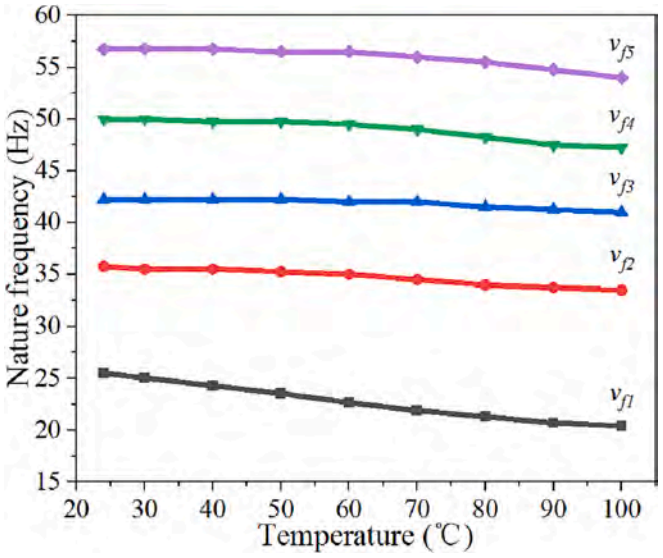

Fig. 12. Natural frequency variations of specimens at different temperatures.

because the change of temperature has a greater effect on the epoxy matrix and a smaller effect on the carbon fiber layer. It can be seen from Fig. 12 that the effect of temperature variation on the dynamic properties of the SMPC structure is smaller when the fiber content is greater than v_{f2}. Therefore, when vibration control is performed on structures with high fiber content, temperature variations have less effect on the vibration suppression effect of the structure. Conversely, when the fiber content is less than v_{f2}, the change of temperature has a greater effect on the dynamic characteristics of the structure, which is not conducive to the vibration control of the structure.

4.3. Open loop control experiment

The experiments were conducted using MFC for active control of SMPC specimens. The overall size of the MFC was 38 mm × 20 mm, and the actuation size was 28 mm × 14 mm. The position coordinates of the MFC actuator arex_1 = 10 mm andx_2 = 38 mm respectively. The electrostatic capacity of the MFC was 1.10 nF, the maximum displacement was 43.4 μm, and the maximum output was 190 N. The input signal voltage for the MFC was −2.5 V-2.5 V. The input peak-to-peak voltage for the shaker is 5 Vpp, and the input peak-to-peak voltage of the MFC was 0.5 Vpp. To maximize the vibration effect of the shaker and MFC on the SMPC specimen, the natural frequency of each experimental specimen was selected as the frequency of the external input sinusoidal signal to obtain the vibration effect of different experimental specimens.

From Fig. 13, it can be seen that the vibration effect of the specimen tends to decrease when the carbon fiber content in the experimental specimen increases under the action of external excitation and MFC. The SMPC specimen with a v_{f1} carbon fiber content is more easily affected by external excitation and is also easier to control. To explore the effect of SMPC specimens under open-loop vibration control, experimental results of open-loop control under different conditions were obtained by adjusting the phase of two input signals of shaker and MFC. The vibration suppression rate for vibration active control is defined as follows:

$$\text{Suppression ratio (\%)} = \frac{D_b - D_a}{D_b} \times 100.$$

where D_b and D_a represent the peak-valley amplitude before suppression and the peak-valley amplitude after suppression, respectively.

The open-loop experiment starts by turning on the exciter and then adding the MFC control. The phase differences for the two input signals are 0°, 90°, 180°, 270° and 360°. After that, the MFC control is removed,

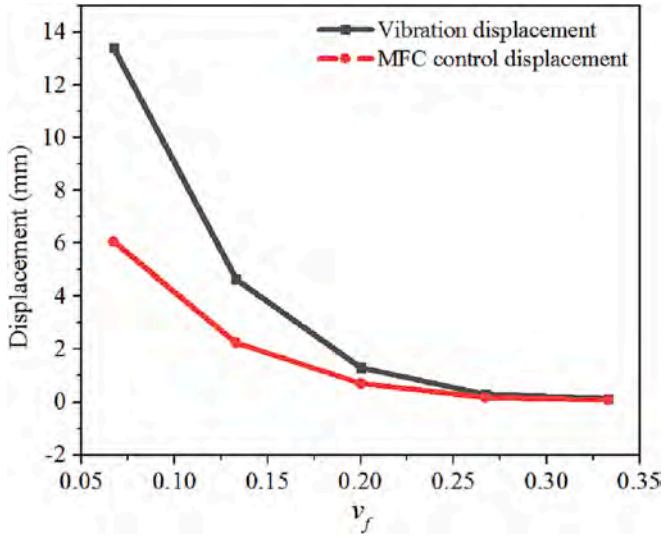

Fig. 13. Displacement diagram of the free end of the SMPC specimens under the action of the shaker and MFC.

and finally the exciter is turned off to complete the open-loop experiment. Finally, the laws of increasing and suppressing the vibration displacement of the free end of the SMPC specimen were obtained. The obtained results are shown in Fig. 14.

It can be observed from Table 4 that the SMPC with v_{f1} has the best vibration control suppression under open-loop control. The maximum vibration suppression rate is 46.294%. With increasing of v_f, the material stiffness of the SMPC increases and the control effect of the open loop gradually weakens. For a carbon fiber content of v_{f5}, the open-loop control effect is the weakest and the vibration suppression rate is 16.901%. After fitting the data in the Table 4 nonlinearly, the relationship between carbon fiber volume content and vibration suppression rate was obtained. The lower the fiber content of the material, the better the vibration suppression effect. The nonlinear fitting analysis of the data shows that the vibration suppression rate is greater than 20% when v_f is less than 0.314. When v_f is less than 0.190, the vibration suppression rate is more than 30%. When v_f is less than 0.149, the vibration suppression rate is more than 40%.

4.4. PID active control

4.4.1. Sweep frequency vibration suppression experiment

In order to achieve a better control effect, when closed-loop control is used for vibration control of the structure, the main focus is on the damping effect of the structure at the natural frequency. During the control process, the PID controller only receives the vibration signal of the specimen at the intrinsic frequency because the filter frequency of the PID filter is adjusted to the intrinsic frequency of the SMPC specimen. The PID controller receives the signal and immediately triggers the MFC controller to perform vibration control on the structure. Therefore, during the sweep vibration, the amplitude of the SMPC specimen at the first resonance peak is suppressed, and the amplitude at the resonance peak shows an abrupt decay as shown in Fig. 15.

The suppression effect of active vibration control is different for SMPC specimens with varying v_f. The attenuation at the first resonance peak is approximately 0.06 mm/N for SMPC specimen with v_{f1}. The attenuation at its the resonance peak is approximately 0.106 mm/N for

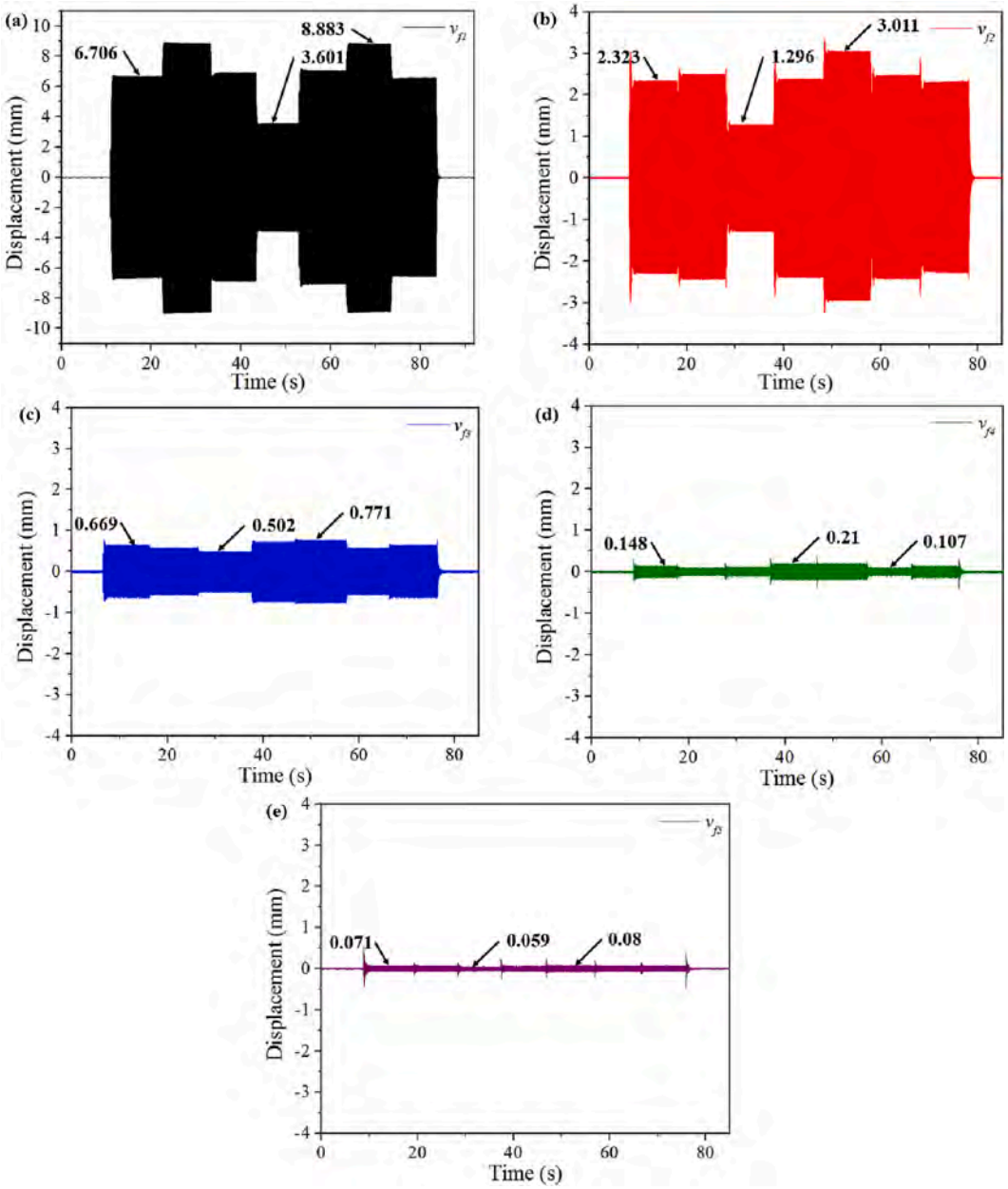

Fig. 14. Open-loop control experiment for SMPC specimens, (a) specimen of v_{f1}, (b) specimen of v_{f2}, (c) specimen of v_{f3}, (d) specimen of v_{f4}, (e) specimen of v_{f5}.

Table 4
Experimental data for open-loop control of SMPC specimens.

Proportion	Vibration displacement /mm	MFC control displacement /mm	Maximum peak-valley amplitude /mm	Minimum peak-valley amplitude /mm	vibration suppression rate
v_{f1}	13.412	6.069	17.766	7.203	46.294%
v_{f2}	4.647	2.249	6.022	2.593	44.201%
v_{f3}	1.338	0.711	1.543	1.005	27.594%
v_{f4}	0.296	0.181	0.421	0.214	27.702%
v_{f5}	0.142	0.09	0.16	0.118	16.901%

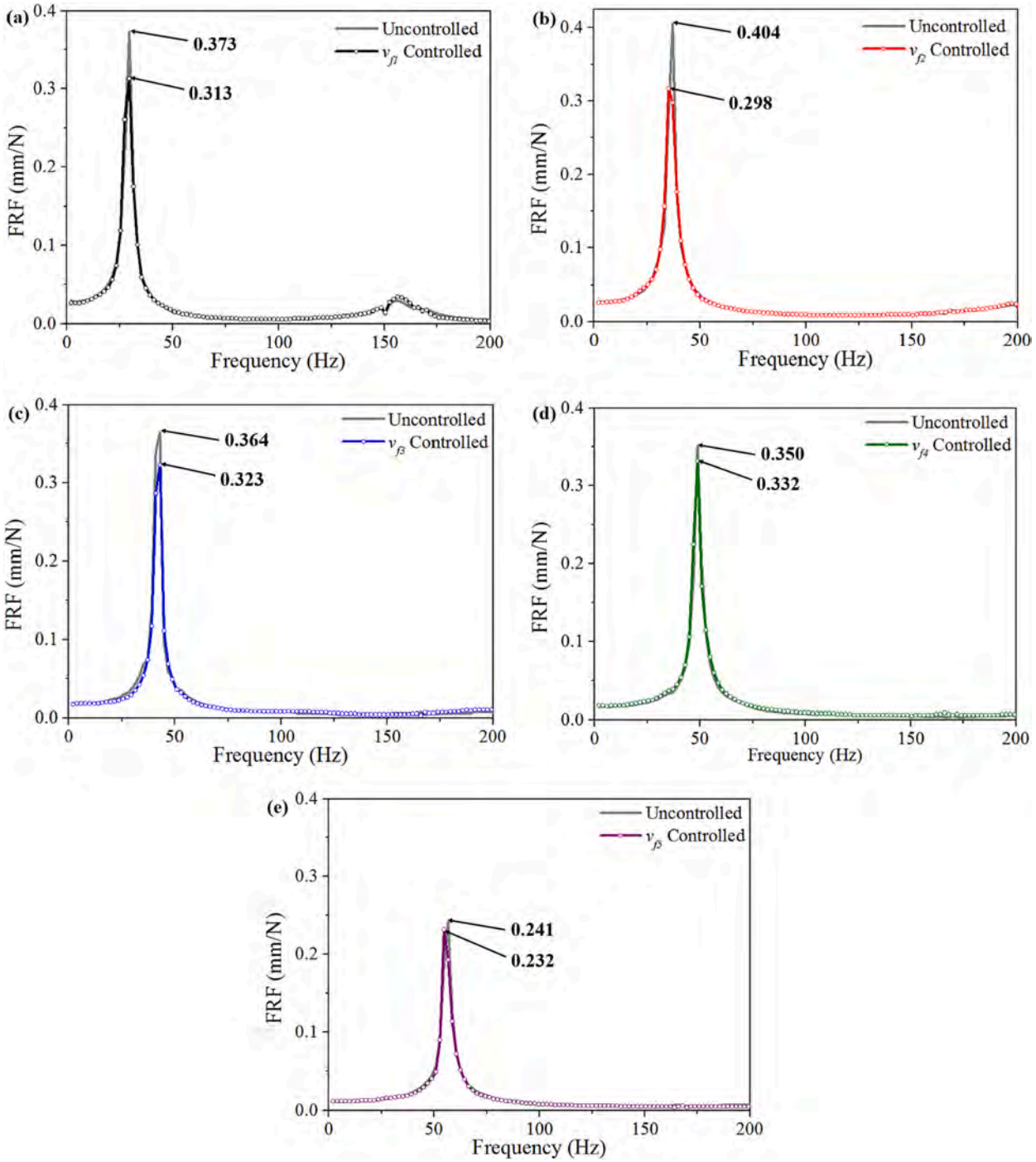

Fig. 15. Uncontrolled and controlled frequency response curves for the SMPC specimens, (a) specimen of v_{f1}, (b) specimen of v_{f2}, (c) specimen of v_{f3}, (d) specimen of v_{f4}, (e) specimen of v_{f5}.

SMPC specimen with v_{f2}. The attenuation at the first resonance peak is approximately 0.041 mm/N for SMPC specimen with v_{f3}. The attenuation at the first resonance peak is approximately 0.018 mm/N for SMPC specimen with v_{f4}. The attenuation at the first resonance peak is approximately 0.009 mm/N for SMPC specimen with v_{f5}. It can be concluded from Fig. 15 that a better swept frequency vibration suppression effect is obtained for SMPC with a carbon fiber content of v_{f2}. The inhibition at the first resonance peak rate can reach a value of 26.238%.

4.4.2. Experimental test

For SMPC specimens with varying v_f, the natural frequency of the vibration exciter was selected as the frequency of the external input si-

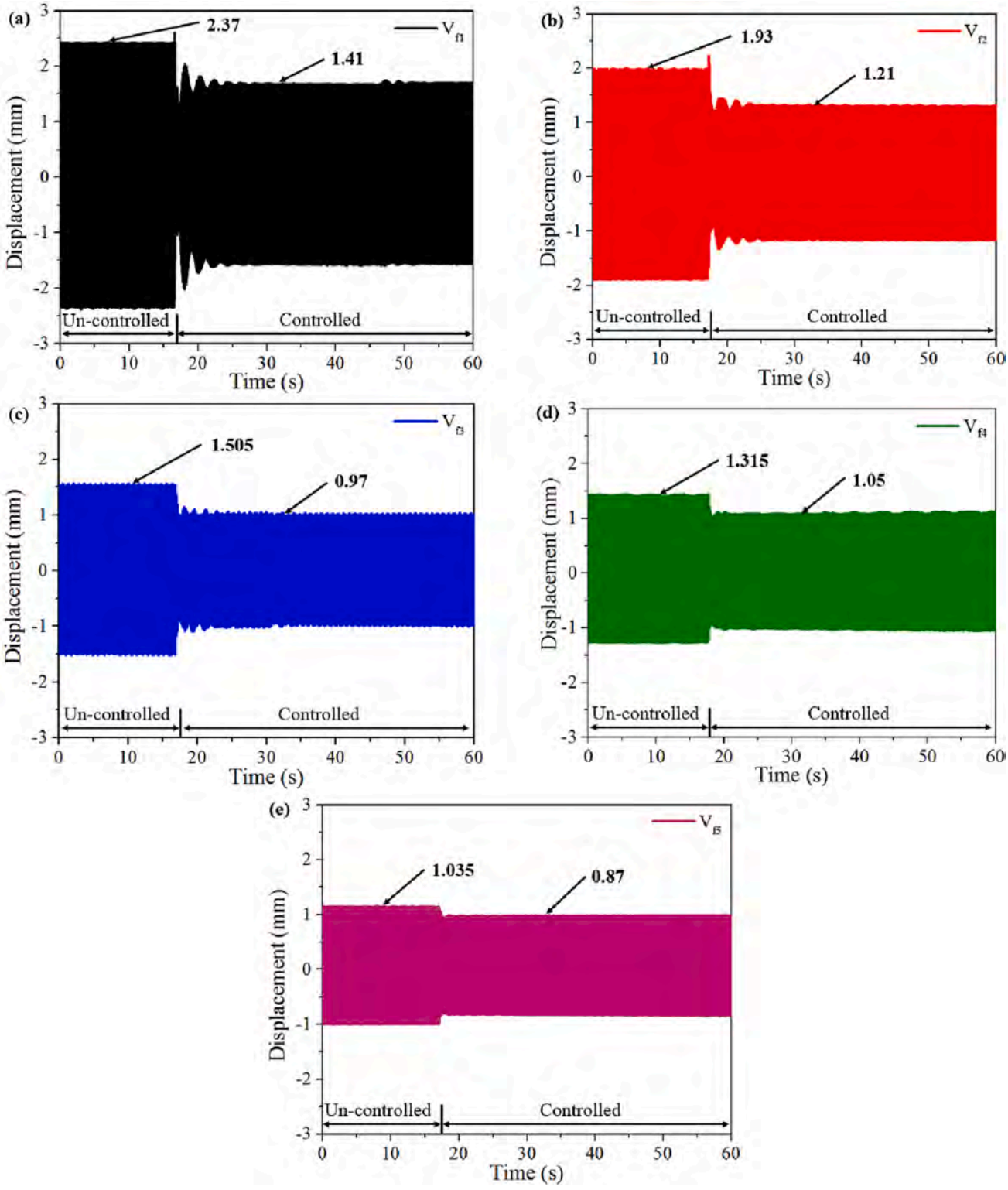

Fig. 16. PID active vibration control experimental diagram for SMPC specimens, (a) specimen of v_{f1}, (b) specimen of v_{f2}, (c) specimen of v_{f3}, (d) specimen of v_{f4}, (e) specimen of v_{f5}.

nusoidal signal. To produce a better active control effect with the MFC, the vibration of the SMPC specimen was actively controlled by using the input signal from classical PID control. The final values used in the experiment were$K_P^* = 1.0$, K_I^*=1.0 and$K_D^* = 0$. The experimental results obtained for active vibration control are shown in Fig. 16.

Table 5 shows that the vibration suppression rates for the SMPC specimens of v_{f1}, v_{f2} and v_{f3} range between 35% and 40%, and the suppression effect is good. The vibration suppression rate for the SMPC specimens of v_{f4} and v_{f5} shows a significant decrease. After fitting the data in the Table 5 nonlinearly, the relationship between carbon fiber volume content and vibration suppression rate was obtained. The lower the fiber content of the material, the better the vibration suppression effect. The nonlinear fitting analysis of the data shows that the vibration suppression rate is greater than 20% when v_f is less than 0.269. When v_f is less than 0.224, the vibration suppression rate is more than 30%. When v_f is less than 0.077, the vibration suppression rate is more than 40%. With a smaller proportion of carbon fiber, the SMPC specimens are more easily affected by external excitation, and they are also easier to control.

To better understand the convergence rate of the system under the closed-loop control system, the convergence time and convergence speed of SMPC specimens with varying v_f were calculated in Table 6, and the obtained data were plotted in Fig. 17. From Fig. 17, the convergence rate of SMPC specimens shows an inverse S-shape with the increase of v_f. When the fiber content v_f is around 0.17, the convergence rate of SMPC specimens is higher, indicating that SMPC specimens at this fiber content are easier to control.(SEE Table 7.).

4.4.3. Simulation

The experimentally determined vibration displacement of the SMPC specimen is used as the basic vibration displacement for the simulation control. According to the state-space equations of the system, the classical PID procedure is used to simulate the active control of vibration for the SMPC specimen.

As shown in Fig. 18, the SMPC is excited to generate fundamental vibrations before the SMPC is actively controlled. After that, the displacement signal is collected by a laser rangefinder located at the free end of the SMPC specimen, and the collected signal is adjusted by the PID control program and transmitted to the MFC actuator. The MFC actuator converts the received signal into the driving force of the SMPC structure. By comparing the simulated data with the experimental data, the simulation data is basically consistent with the experimental data, which proves the correctness of the experiment.

5. Conclusion

Based on Kirchhoff's plate theory, the motion differential equations for composite laminates were derived. The vibration differential equation of the SMPC cantilever plate was obtained by using the separation variable method and the mode shape superposition principle. The state space equation for the system is obtained according to the transfer function. The SMPC specimens with varying v_f were excited by a sinusoidal frequency sweep, and the frequency responses of the SMPC specimens with varying v_f were determined. From the obtained results, the peak of the frequency response function is consistent with the theoretically calculated natural frequency. Under open loop control, SMPC with v_f around 0.067 has the best effect on vibration control and suppression. With increasing v_f, the material stiffness of the SMPC is increased, and the control effect of the open loop is gradually weakened. Under open loop control, SMPC with fiber content around 0.333 has the weakest effect on vibration control and suppression. The classical PID control method was used to study the active control of sweep frequency vibration of SMPC specimens with varying v_f.The results showed that the best sweeping vibration suppression of SMPC was achieved when the v_f was about 0.133. The inhibition rate at the first resonance peak reaches a value of 26.238%.

Finally, the closed-loop vibration control effect of SMPC specimens under natural frequency vibration is investigated. The vibration suppression rates of the SMPC specimens with carbon fiber proportion between 0.067 and 0.200 range between 35% and 40%, and the suppression effect is good. The vibration suppression rate of the SMPC specimens with carbon fiber proportions between 0.200 and 0.333 is significantly decreased. By comparison with the experimental data, it can be found that the simulation data is basically consistent with the experimental data, which proves the correctness of the theoretical

Table 5
PID vibration active control experimental data statistics.

Proportion	Peak-valley amplitude before suppression/mm	Peak-valley amplitude after suppression/mm	PID vibration suppression rate
v_{f1}	4.74	2.82	40.51%
v_{f2}	3.86	2.42	37.31%
v_{f3}	3.01	1.94	35.55%
v_{f4}	2.63	2.10	20.15%
v_{f5}	2.07	1.74	15.94%

Table 6
Convergence time and convergence speed of SMPC specimens.

Proportion	Time to begin convergence/s	Time to end convergence/s	Convergence time/s	convergence speed/mm/s
v_{f1}	16.6	29.5	12.9	0.149
v_{f2}	17.5	26.2	8.7	0.166
v_{f3}	17.0	23.5	6.5	0.165
v_{f4}	17.9	22.3	4.4	0.120
v_{f5}	17.2	19.8	2.6	0.127

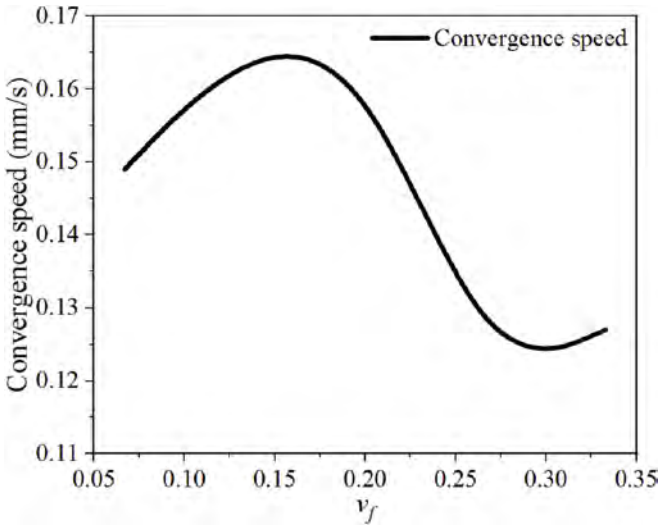

Fig. 17. Convergence speed curve of SMPC specimens.

Table 7
PID vibration active control simulated data statistics.

Proportion	Peak-valley amplitude before suppression/mm	Peak-valley amplitude after suppression/mm	PID vibration suppression rate
v_{f1}	4.80	2.80	41.67%
v_{f2}	3.80	2.40	36.84%
v_{f3}	3.00	1.96	34.67%
v_{f4}	2.60	2.00	23.08%
v_{f5}	2.00	1.74	13.00%

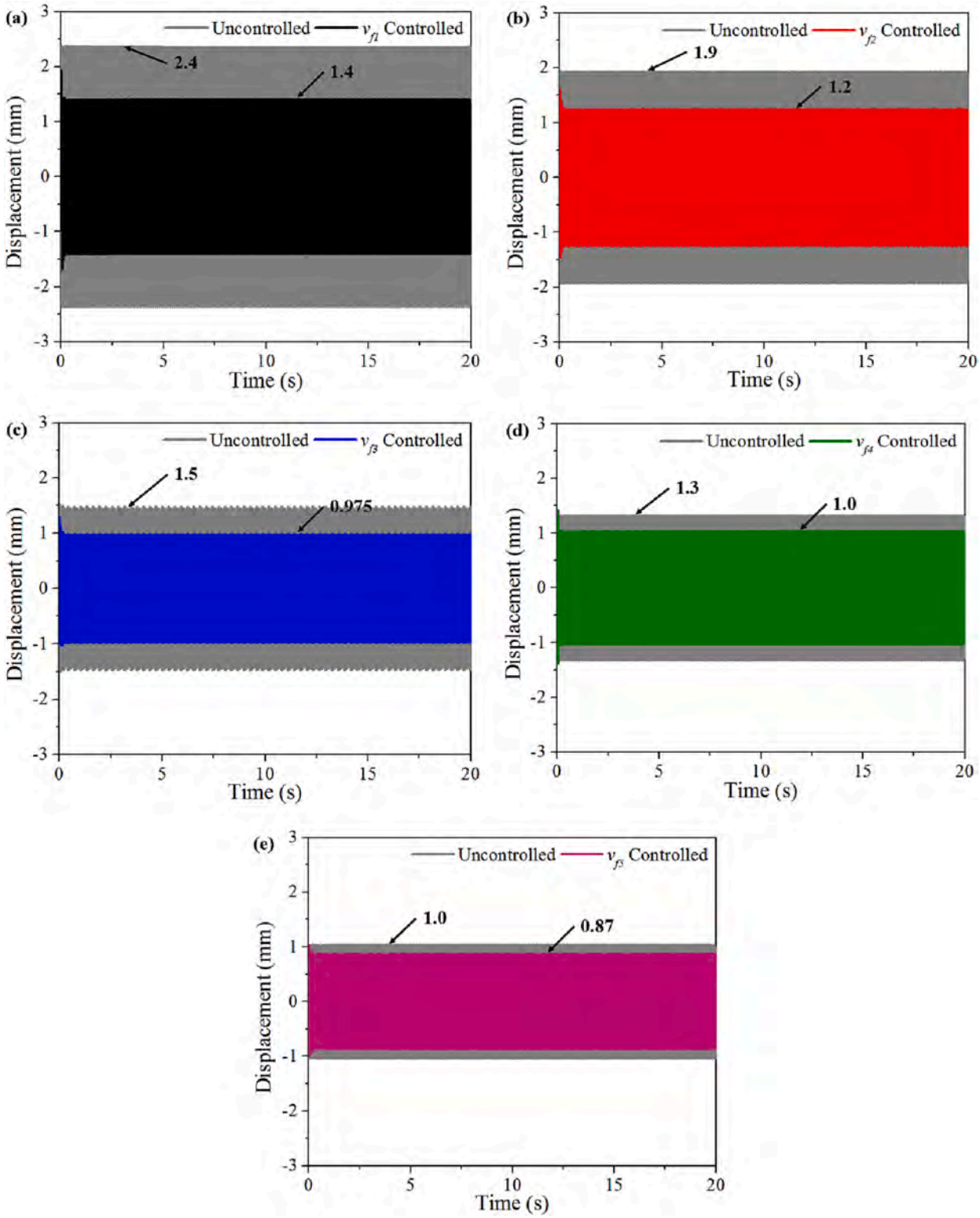

Fig. 18. PID active vibration control simulated diagram for the SMPC specimens, (a) specimen of v_{f1}, (b) specimen of v_{f2}, (c) specimen of v_{f3}, (d) specimen of v_{f4}, (e) specimen of v_{f5}.

calculation results. When the fiber content v_f is around 0.17, the convergence rate of SMPC specimens is higher, indicating that SMPC specimens at this fiber content are easier to control. This is important for the application of a SMPC in a complex space environment.

CRediT authorship contribution statement

Peilei Xu: Conceptualization, Investigation, Visualization, Formal analysis, Writing – original draft, Writing – review & editing. **Xin Lan:** Methodology, Data curation, Validation, Writing – review & editing. **Chengjun Zeng:** Visualization, Data curation, Writing – review &

editing. **Xudong Zhang:** Visualization, Data curation, Writing – review & editing. **Yanju Liu:** Investigation, Writing – review & editing, Supervision. **Jinsong Leng:** Conceptualization, Investigation, Writing – review & editing.

Declaration of Competing Interest

The authors declare that they have no known competing financial interests or personal relationships that could have appeared to influence the work reported in this paper.

Data availability

Data will be made available on request.

Appendix A

According to the boundary conditions of the cantilever plate, it can be determined that:

$$X_m(x) = \cosh(k_m x) - \cos(k_m x) - \frac{\sinh(k_m l) - \sin(k_m l)}{\cosh(k_m l) + \cos(k_m l)} \times [\sinh(k_m x) - \sin(k_m x)], \tag{31}$$

$$Y_n(y) = \begin{cases} 1, & \\ \sqrt{3}\left(1 - \dfrac{2y}{l}\right), & n = 1, \\ & n = 2, \\ \sin(k_n y) - \sinh(k_n y) - \dfrac{\cos(k_n l) - \cosh(k_n l)}{\sin(k_n l) + \sinh(k_n l)} & n \geqslant 3, \\ \times [\cos(k_n y) - \cosh(k_n y)], & \end{cases} \tag{32}$$

Appendix B

The system matrix is

$$A = \begin{bmatrix} 0_{n\times n} & I_{n\times n} \\ -\Omega^2 & -2\zeta_i\Omega \end{bmatrix} \tag{33}$$

The system control matrix is given by

$$B = \begin{bmatrix} 0_{1\times n} & \frac{P\left(W_1'(x_2) - W_1'(x_1)\right)}{M_1} & \frac{P\left(W_2'(x_2) - W_2'(x_1)\right)}{M_2} & \cdots & \frac{P\left(W_n'(x_2) - W_n'(x_1)\right)}{M_n} \end{bmatrix}^T \tag{34}$$

And the system output matrix is

$$C = [\, W_1(x_e) \quad W_2(x_e) \quad \cdots \quad 0_{1\times n} \,] \tag{35}$$

where $\Omega = diag[\omega_1 \quad \omega_2 \quad \cdots \quad \omega_n]$. x_e represents the system output point.

Appendix C

The system matrix is

$$A = \begin{bmatrix} 0_{n\times n} & I_{n\times n} \\ -\Omega^2 & -2\zeta_i\Omega \end{bmatrix} \tag{36}$$

The system control matrix is given by

$$B = \begin{bmatrix} 0_{1\times n} & \frac{W_1(x_3)}{M_1} & \frac{W_2(x_3)}{M_i} & \cdots & \frac{W_n(x_3)}{M_n} \end{bmatrix}^T \tag{37}$$

And the system output matrix is

$$C = [\, W_1(x_e) \quad W_2(x_e) \quad \cdots \quad 0_{1\times n} \,] \tag{38}$$

where $\Omega = diag[\omega_1 \quad \omega_2 \quad \cdots \quad \omega_n]$. x_e represents the system output point.

References:

[1] Leng JS, Lan X, Liu YJ, Du SY. Shape-memory polymers and their composites: Stimulus methods and applications. Prog Mater Sci 2011;56:1077–135.

[2] Zhang FH, Wen N, Wang LL, Bai YQ, Leng JS. Design of 4D printed shape-changing tracheal stent and remote controlling actuation. International Journal of Smart and Nano Materials 2021;12:375–89.

[3] Lendlein A, Jiang HY, Junger O, Langer R. Light-induced shape-memory polymers. Nature 2005;434:879–82.
[4] Zhang HJ, Xia HS, Zhao Y. Light-controlled complex deformation and motion of shape-memory polymers using a temperature gradient. ACS Macro Lett 2014;3:940–3.
[5] Beloshenko VA, Varyukhin VN, Voznyak YV. The shape memory effect in polymers. Usp Khim 2005;74:285–306.
[6] Gunes IS, Jana SC. Shape memory polymers and their nanocomposites: A review of science and technology of new multifunctional materials. J Nanosci Nanotechnol 2008;8:1616–37.
[7] Lendlein A, Kelch S. Shape-memory polymers. Angewandte Chemie-International Edition 2002;41:2034–57.
[8] Zhao F, Zheng XY, Zhou SC, Zhou B, Xue SF, Zhang Y. Constitutive model for epoxy shape memory polymer with regulable phase transition temperature. International Journal of Smart and Nano Materials 2021;12:72–87.
[9] Liu YJ, Du HY, Liu LW, Leng JS. Shape memory polymers and their composites in aerospace applications: a review. Smart Mater Struct 2014;23.
[10] Zhang RR, Guo XG, Liu YJ, Leng JS. Theoretical analysis and experiments of a space deployable truss structure. Compos Struct 2014;112:226–30.
[11] Lendlein A, Langer R. Biodegradable, elastic shape-memory polymers for potential biomedical applications. Science 2002;296:1673–6.
[12] Lan X, Liu YJ, Lv HB, Wang XH, Leng JS, Du SY. Fiber reinforced shape-memory polymer composite and its application in a deployable hinge. Smart Mater Struct 2009;18.
[13] Dao TD, Goo NS, Yu WR. Blocking force measurement of shape memory polymer composite hinges for space deployable structures. J Intell Mater Syst Struct 2018;29:3667–78.
[14] Lan X, Liu LW, Zhang FH, Liu ZX, Wang LN, Li QF, et al. World's first spaceflight on-orbit demonstration of a flexible solar array system based on shape memory polymer composites. Science China-Technological Sciences 2020;63:1436–51.
[15] Wang CG, Wang YF. The mechanical design of a hybrid intelligent hinge with shape memory polymer and spring sheet. Composites Part B-Engineering 2018;134:1–8.
[16] Herath H, Epaarachchi JA, Islam MM, Al-Azzawi W, Leng J, Zhang F. Structural performance and photothermal recovery of carbon fibre reinforced shape memory polymer. Compos Sci Technol 2018;167:206–14.
[17] Santo L, Quadrini F, Bellisario D. Shape memory composite antennas for space applications. 20th Innovative Manufacturing Engineering and Energy Conference (IManEE). Kallithea, GREECE2016.
[18] Ming GQ, Liu LW, Liu YJ, Leng JS. Space deployable parabolic reflector based on shape memory polymer composites. Compos Struct 2023;304.
[19] AIAA. Qualification of elastic memory composite hinges for spaceflight applications; 2006.
[20] Liu YJ, Wang XH, Lan X, Lv HB, Leng JS. Shape memory polymer composite and its application in deployable hinge for space structure. Conference on Sensors and Smart Structures Technologies for Civil, Mechanical, and Aerospace Systems. San Diego, CA2008.
[21] Liu TZ, Liu LW, Yu M, Li QF, Zeng CJ, Lan X, et al. Integrative hinge based on shape memory polymer composites: Material, design, properties and application. Compos Struct 2018;206:164–76.
[22] Liu ZX, Lan X, Bian WF, Liu LW, Li QF, Liu YJ, et al. Design, material properties and performances of a smart hinge based on shape memory polymer composites. Composites Part B-Engineering 2020:193.
[23] Lan X, Liu LW, Pan CT, Li FF, Liu ZX, Hou GH, et al. Smart solar array consisting of shape-memory releasing mechanisms and deployable hinges. AIAA J 2021;59:2200–13.
[24] Zhang D, Liu LW, Lan X, Leng JS, Liu YJ. Synchronous deployed design concept triggered by carbon fibre reinforced shape memory polymer composites. Compos Struct 2022;290.
[25] Zhang D, Liu LW, Xu PF, Zhao YZ, Li QF, Lan X, et al. Ancient papyrus scroll-inspired self-deployable mechanism based on shape memory polymer composites for Mars explorations. Compos Struct 2023;304.
[26] Qiu ZC, Zhang XM, Wu HX, Zhang HH. Optimal placement and active vibration control for piezoelectric smart flexible cantilever plate. J Sound Vib 2007;301:521–43.
[27] Hagood N, Kindel R, Ghandi K, Gaudenzi P. Improving transverse actuation of piezoceramics using tnterdigitated surface electrodes. 1993 Smart Structures And Materials Conf : Smart Structures And Intelligent Systems. Albuquerque, Nm1993. p. 341-52.
[28] Leng JS, Xie F, Wu XL, Liu YJ. Effect of the gamma-radiation on the properties of epoxy-based shape memory polymers. J Intell Mater Syst Struct 2014;25:1256–63.
[29] Elliott SJ. Distributed control of sound and vibration. Noise Control Engineering Journal 2005;53:165–80.